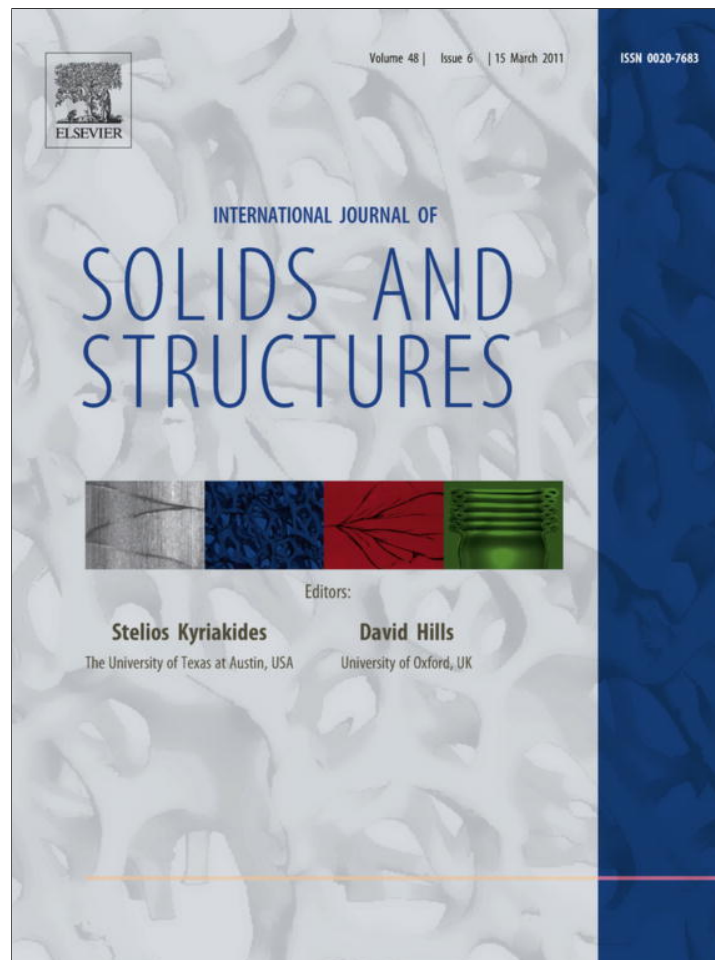


Provided for non-commercial research and education use.
Not for reproduction, distribution or commercial use.



This article appeared in a journal published by Elsevier. The attached copy is furnished to the author for internal non-commercial research and education use, including for instruction at the authors institution and sharing with colleagues.

Other uses, including reproduction and distribution, or selling or licensing copies, or posting to personal, institutional or third party websites are prohibited.

In most cases authors are permitted to post their version of the article (e.g. in Word or Tex form) to their personal website or institutional repository. Authors requiring further information regarding Elsevier's archiving and manuscript policies are encouraged to visit:

<http://www.elsevier.com/copyright>



Contents lists available at ScienceDirect

International Journal of Solids and Structures

journal homepage: www.elsevier.com/locate/ijsolstr

The effects of the interphase and strain gradients on the elasticity of layer by layer (LBL) polymer/clay nanocomposites

Yaning Li^{a,*}, Anthony M. Waas^b, Ellen M. Arruda^c

^a Department of Mechanical Engineering, Massachusetts Institute of Technology, Cambridge, MA 02139-4307, USA

^b Department of Aerospace Engineering, University of Michigan, Ann Arbor, MI 48109-2140, USA

^c Department of Mechanical Engineering, University of Michigan, Ann Arbor, MI 48109-2125, USA

ARTICLE INFO

Article history:

Received 8 March 2010

Received in revised form 14 October 2010

Available online 16 December 2010

Keywords:

Polymer/clay

Nanocomposites

Interphase

Strain gradient

Finite element

Mori–Tanaka model

Size effect

ABSTRACT

A synergistic stiffening effect observed in the elastic mechanical properties of LBL assembled polymer/clay nanocomposites is studied via two continuum mechanics approaches. The nanostructure of the representative volume element (RVE) includes an effective interphase layer that is assumed to be perfectly bonded to the particle and matrix phases. An inverse method to determine the effective thickness and stiffness of the interphase layer using finite element (FE) simulations and experimental data previously published in Kaushik et al. (2009), is first illustrated. Next, a size-dependent strain gradient Mori–Tanaka (M–T) model (SGMT) is developed by applying strain gradient elasticity to the classical M–T method. Both approaches are applied to LBL-assembled polyurethane–montmorillonite (PU–MTM) clay nanocomposites. Both two-dimensional (2D) and three-dimensional (3D) FE models used in the first approach are shown to be able to accurately predict the stiffness of the PU–MTM specimens with various volume fractions. The SGMT model also accurately predicts the experimentally observed increase in stiffness of the PU–MTM nanocomposite with increasing volume fraction of clay. An analogy between the strain gradient effect and the role of an interphase in accounting for the synergistic elastic stiffening in nanocomposites is provided.

© 2010 Elsevier Ltd. All rights reserved.

1. Introduction

Polymer/clay nanocomposites, as members of the organic–inorganic nanocomposite family, are promising materials exhibiting attractive hybrid physical and mechanical properties arising from synergistic effects among their components. The nanocomposites show improved mechanical properties over microcomposites with similar micro-structure. Although this can be partially attributed to the high stiffness of nanoparticles, the improved bonding between bulk polymer matrix and the surfaces of the fillers due to the high surface-to-volume ratio at the nanoscale also contributes to this improvement. The influence of the interphase, a region between the polymer matrix and the filler surfaces with substantially modified polymer chain conformational states caused by molecular interactions with the reinforcement phase, is perhaps the main contributor to the enhancement of the nanocomposite mechanical properties (Pukanszky, 2005; Putz et al., 2008; Ginzburg and Balazs, 1999; Liu et al., 2004; Ciprari et al., 2006). A recent study of the influence of the filler to matrix stiffness ratios (SRs) on nanocomposite enhancement efficiency showed an asymptotic upper limit to the increased enhancement efficiency with increasing

SRs (Li et al., 2011). This previous analysis demonstrated that without a finite thickness interphase region, large values of SR result in no substantially improved enhancement. Many existing nanocomposites have SRs that have reached this limit. Therefore, in order to further optimize the mechanical properties of nanocomposites, an examination of the role of the interphase becomes important for nanocomposite design.

The present study focuses on a type of nanocomposite formed via LBL assembly of polymer and clay nanoparticles (Podsiadlo et al., 2007, 2008; Li et al., 2008a,b,c; Kaushik et al., 2009). The experimental results from a family of LBL polyurethane–montmorillonite (PU–MTM) clay nanocomposites (Kaushik et al., 2009) are used. The nanostructures of these LBL PU–MTM clay nanocomposites are studied in Section 2.

Classical two-phase micro-mechanical models, such as the Mori–Tanaka (M–T) model (Mori and Tanaka, 1973; Tandon and Weng, 1984) and the Halpin–Tsai (H–T) model (Halpin, 1969; Halpin and Kardos, 1976) fail to predict the mechanical stiffness of LBL PU–MTM nanocomposites, as shown in Section 3. A similar observation has been reported by other researchers when applying these models directly to other nanocomposite structures (Sheng et al., 2004; Hbaieb et al., 2007; Liu and Brinson, 2006; Li et al., 2008b). Depending on the components and the manufacturing processes of different types of nanocomposites, the existence of the interphase can be attributed to the gyration of the polymer chain

* Corresponding author. 77 Massachusetts Ave. MIT, Room 1-025, Cambridge, MA 02139-4307, USA.

E-mail address: yaningli@mit.edu (Y. Li).

(Fossey, 2002; Baschnagel and Binder, 1995), the effect of covalent cross-link density (Putz et al., 2008) or the thermodynamic effect (Lipatov and Nesterov, 1997; Ginzburg and Balazs, 1999; Helfand and Tagami, 1972). In Sections 3 and 4, the role of the interphase is examined using continuum mechanics. One approach predicts the stiffness of nanocomposites using the finite element (FE) method by judicious choice of 2D or 3D RVEs. A second approach examines the effect of strain gradients using a modified M–T model, and is illustrated in Sections 5 and 6.

Currently, no reliable experimental method for determining the interphase properties exists, although many efforts have been made (Ginzburg and Balazs, 1999; Liu et al., 2004; Ciprari et al., 2006) to find one. More information about the current status of the study of the role of the interphase in nanocomposite mechanics can be found in a review paper (Pukanszky, 2005). In the present investigation, an inverse method using FE simulations of the nanostructure of the RVE is applied to calibrate the mechanical and physical properties of the interphase using experimental data, and this is shown in Section 3. In Section 4, the synergistic effect of the interphase is analyzed from the FE results, showing how the interphase controls the load transfer between matrix and filler. The analogy between a region with a high strain gradient and a physical interphase is addressed.

Classical elasticity assumes that the stress at a material point is uniquely determined by the strain at that point. Nonlocal elasticity which is a higher order continuum theory of elasticity (Eringen, 1972; Eringen and Edelen, 1972, also a review can be found in Bažant and Cedolin, 1991) argues that the stress at any particular point in a solid is not only determined by the strain at that point but also by the strains of the neighboring points. If the strain gradient is high, classical elasticity is not sufficiently accurate to describe the constitutive behavior of a material and we need to resort to strain gradient theory.

In Section 6, the strain gradient M–T model is developed and is applied to predict the stiffness of the PU–MTM specimens. An alternative strain gradient elasticity theory (Aifantis, 1999; Askes and Aifantis, 2006) is introduced to the Mori–Tanaka model derived in the framework of classical elasticity (Tandon and Weng, 1984). Again, excellent correlation with experimental data is obtained. In addition, it is also shown in Section 6 that the strain gradient M–T model is size-dependent. Strain gradient plasticity has also previously been applied to study the plastic behavior of PU–MTM nanocomposites, as described in Li et al. (2008c).

2. Nanostructure

The LBL PU–MTM clay nanocomposite (Kaushik et al., 2009) is a type of nanocomposite that results in a well-defined spacing between subsequent clay layers by virtue of sequential layering of polymer and clay nanoparticles (Podsiadlo et al., 2007, 2008). An

RVE based on the nanostructure of the PU–MTM nanocomposite is described in this section. The clay particles in the PU–MTM are exfoliated as layers composed of disk or flake-shaped particles dispersed in a PU matrix. Each clay layer is comprised of aligned clay flakes separated by the PU matrix in a manner similar to the brick and mortar structure of nacre (Tang et al., 2007; Barthelat et al., 2007). Specimens with various volume fractions of clay are obtained by changing the thickness of the polymer layers. In reality, the boundaries of the clay particles are irregular, also, the staggering within particle layers is not uniform, but overall, these nanocomposites have a well-defined stratified nanostructure. For simplicity, the nanostructure is idealized by neglecting these irregularities and non-uniformities, as shown in Fig. 1. The idealized nanostructure leads to a feature of in-plane orthotropy, although the real material is in-plane isotropic.

For the PU–MTM nanocomposites, each particle shown in Fig. 1(a) and (b) represents an effective particle that includes a few layers (how the number of layers can be determined will be explained later in this section) of silicate nanoparticles each with a thickness of 1 nm connected by layers of water bridges with a thickness of 0.28 nm (Kaushik et al., 2009); the details of the effective clay particle are shown in Fig. 1b.

Both 2D plane strain and 3D RVEs for FE analysis are chosen based on the idealized nanostructure shown in Fig. 1. For a 2D plane strain RVE, the nanostructure through-the-thickness is shown in Fig. 1(b) by the red and blue squares and the plane strain condition holds in the third direction. For a 3D RVE, in addition to the structure through-the-thickness shown in Fig. 1(b), the structure viewed in the third direction is shown in Fig. 1(a) by the red and blue squares. There are many ways of choosing the RVEs, which can be generalized into two types: symmetric (shown by the red squares C or D in Fig. 1) or unsymmetric (shown by the blue squares A or B in Fig. 1). An unsymmetric RVE is recommended for FE simulation with periodic boundary conditions (PBC), because when applying PBCs, the symmetric structure will conflict with the PBC and lead to inaccurate simulation results, as also reported by Hbaieb et al. (2007). The details of the unsymmetric through-the-thickness cross section of the RVE are shown in Fig. 2.

In Fig. 2, L_c is the length of the RVE, t_c is the thickness of the RVE, t_p is the thickness of the effective clay particle, L_p is the length of the effective clay particle, and t_b is the bilayer thickness, defined as the distance between the mid-planes of two neighboring clay layers. For the LBL PU–MTM nanocomposites, an average L_p was measured using light scattering (Zetasizer) and the average t_b , by scanning electron microscopy (SEM). L_p is 110 nm and t_b varies with different volume fractions of clay, reported by Kaushik et al. (2009). The unknown independent dimensions are t_p , L_c and t_i (the thickness of the assumed uniform effective interphase), which cannot be measured from the experiments. In this section, we will illustrate how to determine t_p and L_c by analyzing the

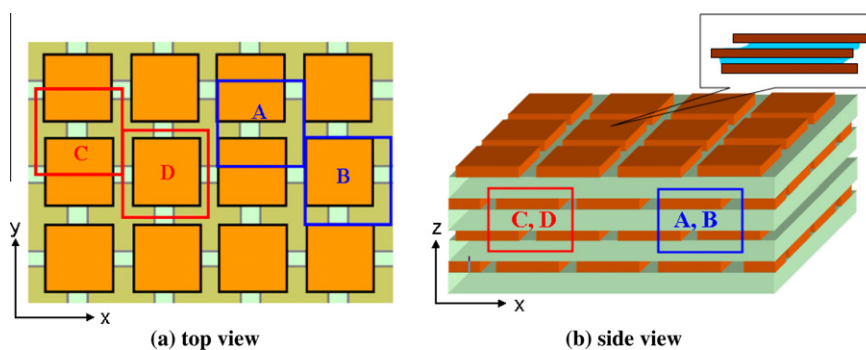


Fig. 1. Sketch of the idealized nanostructure of an LBL nanocomposite (brown squares represent clay particles, green layers are polymer layers). (For interpretation of the references to colour in this figure legend, the reader is referred to the web version of this article.)

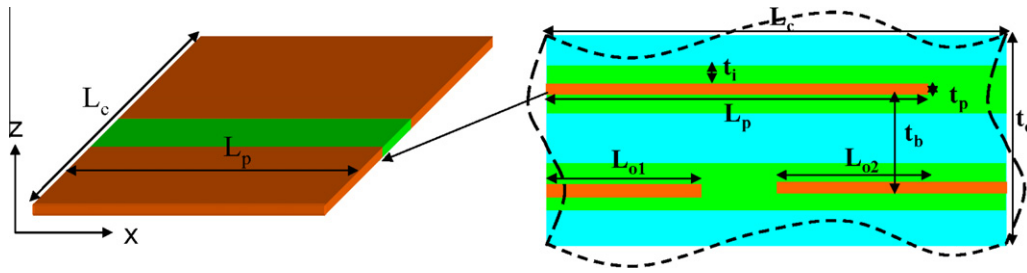


Fig. 2. Dimensions of the 2D RVE and/or the through-thickness cross-section of the 3D RVE.

nanostructure. L_{o1} and L_{o2} are the staggering lengths between clay layers. Fertig and Garnich (2004) studied the influence of the staggering factor (L_{o1}/L_p) ranging from 0 to 1, and showed that the staggering factor has a small effect on exfoliated nanocomposites. For the present idealized nanostructure, $L_{o1} = L_{o2}$ is assumed, indicating that the staggering factor equals $\frac{2L_p - L_c}{2L_p}$. Thus, L_{o1} and L_{o2} are not independent parameters, when the volume fraction is known, they are determined from L_p and L_c . For the LBL polymer/clay nanocomposite, the staggering factor is much larger than 0. It is reasonable to assume the staggering factor is larger than 1/4, since there is only a little gap (less than 0.5 L_p) between neighboring clay particles in a single clay layer. Thus, the independent dimensions of the 3D RVE are related to the volume fraction of the nanocomposites:

$$f_v = \frac{L_p^2 t_p}{L_c^2 t_b}, \quad (1)$$

which indicates:

$$f_v \propto \frac{1}{t_b}. \quad (2)$$

Assuming:

$$f_v = K \left(\frac{1}{t_b} \right), \quad (3)$$

then

$$K = \frac{L_p^2}{L_c^2} t_p. \quad (4)$$

The bilayer thicknesses t_b for PU–MTM specimens with various volume fractions f_v are measured by SEM and reported by Kaushik et al. (2009). Eq. (3) indicates that if the idealized RVE of the nanostructure is correct, the two variables measured, f_v and $\frac{1}{t_b}$, should be linearly related. Also, K in Eq. (3) can be found by linear regression, as shown in Fig. 3, in which the markers are the experimental data reported by Kaushik et al. (2009), the line is obtained by linear regression, and the slope of the line is K , which is found to be 2.17 nm.

Considering that gaps exist between clay particles in the same layer, which indicates $\frac{L_p}{L_c} < 1$, from Eq. (4), we obtain:

$$t_p > K. \quad (5a)$$

Thus, K gives the lower limit of the clay layer thickness.

The upper limit of t_p is determined by the aforementioned staggering factor of clay particles. Since the staggering factor is larger than 1/4, we can get $\frac{L_p}{L_c} > \frac{2}{3}$. From Eq. (4), we obtain:

$$t_p > 2.25K. \quad (5b)$$

Kaushik et al. (2009) observed that small-angle shoulders in the wide angle X-ray scattering response of these nanocomposites which indicates that the effective clay particles include several layers of silicate nanoparticles (1 nm thickness per layer) connected by layers of water bridges (about 0.28 nm thickness per layer).

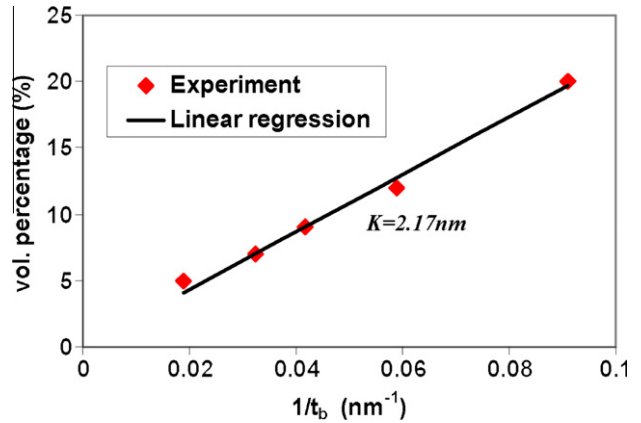


Fig. 3. Proof of the nanostructure model and determination of the minimum particle thickness.

Therefore, from Eqs. (5a) and (5b), we can obtain the number of silicate layers in the effective clay particles. This number is larger than 2 but less than 4. Thus the effective clay particle is determined to be composed of three layers of silicate particles connected by two layers of water bridges, as shown in Fig. 1(b). The thickness of the effective clay particles is therefore determined to be $t_p = 3.6$ nm.

In addition, Eq. (4) yields:

$$L_c = \frac{L_p}{\sqrt{K}} \sqrt{t_p}. \quad (6)$$

Thus, from Eq. (6), the unknown dimension L_c is determined to be 142 nm.

So far, the nanostructure and dimensions of the RVEs are determined. In the following section, the role of the interphase in the enhancement mechanism of the LBL PU–MTM nanocomposites is studied by comparing the FE results of RVE models without an interphase and with an assumed uniform interphase. The interphase properties are determined during this process.

3. Determination of the interphase properties by an inverse FE simulation method

In Kaushik et al. (2009), the in-plane tensile stiffnesses of five PU–MTM specimens with volume fractions 5%, 7%, 9%, 12%, 20% were reported. For FE simulations, the 3D model is more accurate than the 2D model but the 2D model is more efficient computationally. Therefore, in this study, both 2D and 3D simulations are performed and the results are compared with the experimental results.

Both 2D plane strain and 3D FE models using the type A unsymmetric RVE shown in Fig. 1 are constructed in ABAQUS¹ version 6.6.

¹ ABAQUS is a commercially available finite element software package under license to the University of Michigan.

The dimensions of the clay particles and the RVEs have been determined by the nanostructure described in Section 2. Each phase is assumed to be linear elastic and isotropic. The Young's modulus of the effective clay particle is $E_1 = 270$ GPa, (used by Podsiadlo et al. (2007), and can be obtained by the molecular dynamic approach proposed by Manevitch and Rutledge, 2004), the Poisson's ratio of soft clay is 0.375 (Dunn et al., 1980), and that of nano MTM particles were reported to be in a range of 0.2–0.4 in the literature (Cosoli et al., 2008; Suter et al., 2007). Here, we assume the Poisson's ratio of the effective clay particles, $\nu_1 = 0.375$; the Young's modulus of PU is $E_0 = 25$ MPa, and its Poisson's ratio is $\nu_0 = 0.48$ (Qi and Boyce, 2005). As a result of orthotropy, the modulus and Poisson's ratios of the 3D RVE satisfy $E_{xy} = E_{yx}$, $\nu_{xy} = \nu_{yx}$ and $\nu_{yz} = \nu_{zy}$. By simulating the in-plane simple tension of 3D RVEs of various volume fractions, the elastic parameters E_{xy} , ν_{xy} and ν_{xz} for various volume fractions can be obtained. In 2D plane strain RVEs, the clay particle is a combination of the effective clay particle and PU matrix, shown in Fig. 2. Thus the Young's modulus of the clay particle in a 2D RVE is estimated using the rule of mixtures. The contribution of the PU part is negligible. Thus, $E_1^{2D} \approx \frac{t_p}{t_c} E_1 = 209$ GPa. From the 2D simulations of tension loading, the plane strain modulus E_{xy}^{ps} can be obtained. The modulus E_{xy} can be calculated using $E_{xy} = (1 - \nu_{xy}^2) E_{xy}^{ps}$, where ν_{xy} is obtained from the results of the 3D RVEs.

The interphase is assumed to have the same Poisson's ratio as the PU matrix. The thickness t_i and stiffness E_i of the interphase are determined from FE simulations. The strategy of determining E_i and t_i is an inverse approach in which the stiffness of the two-phase RVEs with no interphase is solved both numerically and analytically and is compared with the experimental data. To simulate the mechanical behavior of a nanocomposite specimen by a RVE that is far from its edge, periodic boundary conditions are used in the FE simulations. Nodal constraint equations are used to impose PBCs in ABAQUS. Details of this approach can be found in the recent literature (Sheng et al., 2004; Hbaieb et al., 2007; Tang et al., 2007; Bertoldi et al., 2008).

3.1. Results of the two-phase models with no interphase

Two existing two-phase micro-mechanical composite models, the Mori–Tanaka (M–T) model and the Halpin–Tsai (H–T) model were used by Sheng et al. (2004) to model polymer/clay nanocomposites. The Halpin–Tsai model is an empirical composite model developed by analyzing many FE simulations of different composite configurations as described by Halpin (1969) and Halpin and Kardos (1976). The M–T model uses the concept of average stress, introduced by Mori and Tanaka, who considered the average matrix stress to be perturbed from that of the applied stress due to the presence of the inclusions. Then, the volume averages of the perturbations over the matrix and inclusion volume must vanish to maintain equilibrium. Details of the M–T model are provided in Mori and Tanaka (1973), Tandon and Weng (1984).

In this section, the H–T model, the M–T model and the 2D plane strain and 3D FE models without an interphase are all used to predict the Young's modulus of the PU–MTM specimens at various volume fractions. These predictions are compared with the experimental data reported by Kaushik et al. (2009). A comparison of the modeling and experimental results is made in Fig. 4, in which it is shown that with the assumption of no interphase, all analytical and numerical model predictions are well below the experimental data. Also, the H–T model over-predicts the FE results and the M–T model is consistent with the FE results for small volume fractions but under-predicts the FE results for larger volume fractions. Similar trends are reported in the literature. For example, Sheng et al. (2004) compared the H–T, M–T and 2D plane strain FE results for polymer/clay nanocomposites with volume fractions less than 10%, and a similar conclusion was drawn. Hbaieb et al. (2007)

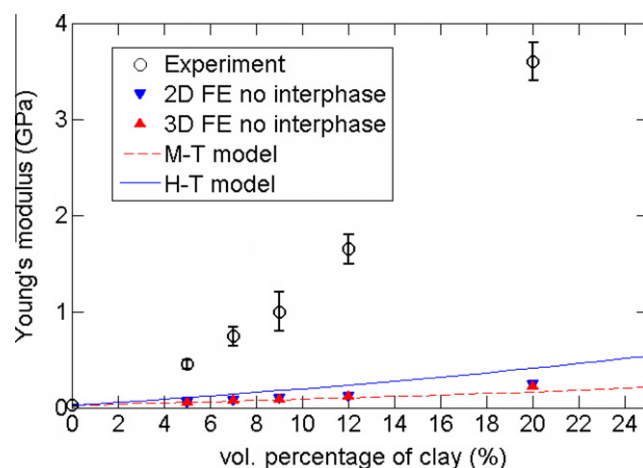


Fig. 4. Comparison of two-phase Mori–Tanaka, Halpin–Tsai, 2D FE and 3D FE simulations to experimental results (Kaushik et al., 2009) (these simulations assume no interphase).

has shown that the M–T model can predict the stiffness of nanocomposites with volume fractions less than 5% but underestimates the stiffness at higher volume fractions. Li et al. (2011) recently demonstrated the same trend when two-phase H–T and M–T models are used to simulate the stiffness of nanocomposites with very high stiffness ratios (SRs) as is the case with the present PU–MTM nanocomposites (SR = 10,000).

The 3D RVE represents the 3D nanostructure of the material and therefore is more accurate than the 2D model. However, all two-phase models with no interphase greatly underestimate the experimental data, as shown in Fig. 4. In the next section, an interphase layer will be introduced to the RVEs. FE simulations are used to determine the properties of the interphase.

3.2. Results of the three phase model with a uniform thickness interphase

The results in Section 3.1 show that unlike microcomposites (such as continuous fiber composites used in the aerospace industry), in which the interphase can be neglected with no substantial influence to the stiffness evaluation, the interphase must be considered in nanocomposites, as also shown in previous work (Fertig and Garnich, 2004; Liu and Brinson, 2006, 2008). Although the interphase thickness should not be a constant size due to the absence of a well-defined border of the interphase with the bulk polymer (Ciprari et al., 2006), we assume an interphase layer around the clay particles with a constant 'effective' thickness to initiate the study. This interphase is also assumed to be an isotropic and linear elastic continuum. The interphase that forms between the polymer and clay layers in the LBL manufacturing process is not dependent upon the clay volume fraction. It is therefore assumed that the value of E_i is independent of volume fraction, as is t_i at low volume fractions, i.e. at clay layer separations greater than $2t_i + t_p$. With an increase in clay volume fraction, the distance between neighboring interphase layers eventually goes to zero and then the material becomes quasi-two-phase: clay particles and interphase. This concept was illustrated by Li et al. (2008b). Kaushik et al. (2009) observed a sharp transition from ductile to brittle response at the clay volume fraction of 12%, thus the specimen with the volume fraction of 12% is assumed to be quasi-two-phase, suggesting that the interphase regions have begun to contact and/or overlap at this volume fraction and the specimens with volume fraction larger than 12% are all approximately quasi-two phase.

The initial Young's modulus of the interphase can therefore be calculated inversely from the M–T model using the experimental data corresponding to the 0.12 volume percent clay. The ratio of the interphase stiffness to the PU matrix stiffness is defined as $nEi = Ei/E0$. The ratio of the interphase thickness to the PU matrix thickness is defined as $nti = ti/t_p$. The result of this inverse calculation with the M–T model gives a value of $nEi = 17$. The simulations of the two-phase model with all matrix replaced with the interphase and using the H–T model, the M–T model, and 2D and 3D FE simulations are compared with the experimental data of Kaushik et al. (2009) in Fig. 5.

From the FE results, it can be concluded that the interphase layers do contact one another when the volume fraction is near 12%, because the two-phase FE results over-predict the stiffness when the volume fraction of the specimen is less than 12%, while for a volume fraction larger than 12%, the FE results are consistent with the experiments, which indicates that the material transforms from three-phase to two-phase as the volume fraction increases beyond 12%. Therefore, the thickness of the interphase can be calibrated at this volume fraction. $nti = 2$ is obtained. Using $nEi = 17$ and $nti = 2$ obtained from the FE calibration results, the 2D and 3D RVEs with constant interphase can predict the stiffness of all specimens, spanning the volume fraction range from 5% to 20%, as seen in Fig. 6(a) and (b). It is worth noting that $nEi = 17$ obtained from the M–T method is only an initial value of the inverse method because when the SR is high, the accuracy of M–T model decreases with the increasing volume fraction (Li et al., 2011). If needed, more accurate values of nEi and nti can be obtained with another round of iteration.

4. The synergistic effect due to interphase

The stress and strain distributions of both 2D and 3D RVEs of various volume fractions are shown in the Appendix A. Since the analysis in this section is conceptual, for simplicity, the 2D results are used. The sketch of the strain distribution between two neighboring clay layers and the coordinate system are shown in Fig. 7.

Taking the case with a volume fraction of 5% as an example, the real strain and stress distributions along z as illustrated in Fig. 7 are shown in Fig. 8. When an interphase is included, the interphase helps redistribute loads between the matrix and the particles; strain in the particles is increased and the strain in the matrix is reduced, as shown in Fig. 8(a). Also, by comparing the peaks of the two curves shown in Fig. 8(b), it is seen that with an interphase,

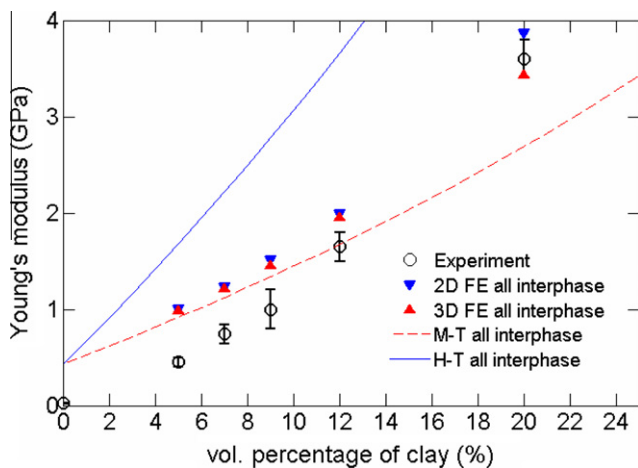


Fig. 5. Comparison of two-phase Mori–Tanaka, Halpin–Tsai, 2D FE and 3D FE simulations to experimental results (Kaushik et al., 2009) (all simulations assume the matrix phase has interphase properties).

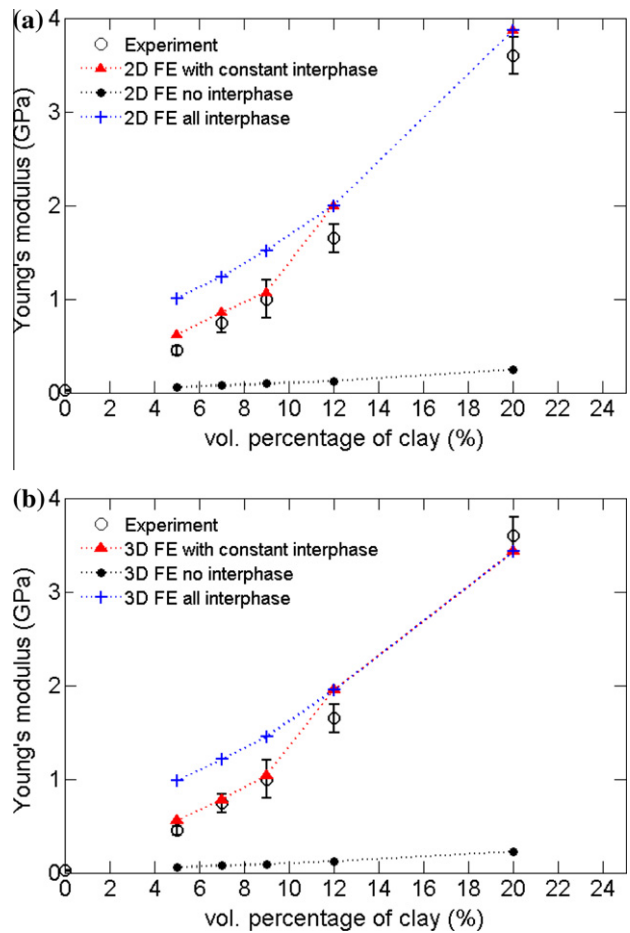


Fig. 6. Comparison of three-phase, FE simulations to experimental results: (a) 2D plane strain FE results, (b) 3D FE results (all simulations assume a constant interphase thickness $nti = 2$ and $nEi = 17$).

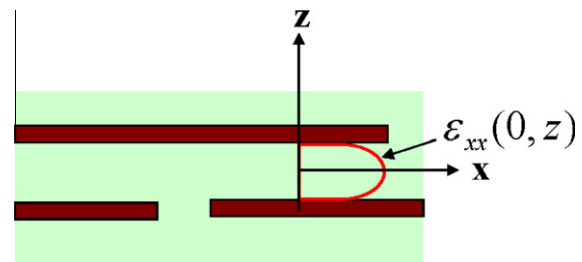


Fig. 7. Sketch of strain distribution between two neighboring clay layers.

the load carried by the clay particles increases more than 6 times. If there is no interphase, clay particles take about 84% load; with an interphase, the load taken by clay particles increases to 98%.

Without the interphase, as the SR increases, the load carrying capability of the particles increases, however, this increase is limited by the particle stiffness, leading to an upper limit of the enhancement efficiency with the increase of SRs (Li et al., 2011). As a metaphor to the old saying ‘the abler a man is, the busier he gets’, although the load carrying ability of the interphase itself and its contribution to the stiffness of the composite is negligibly small, it plays an important role to act as a ‘buffer’ layer, making the ‘abler’ clay get even ‘busier’. Therefore, much more improved enhancement efficiency can be achieved due to this distinct ability of the interphase in controlling load transfer.

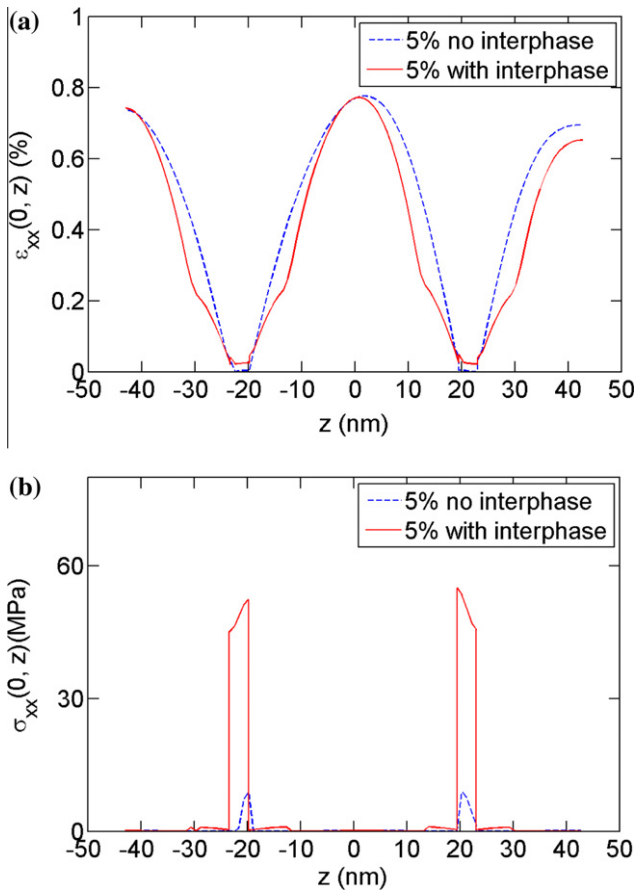


Fig. 8. Comparison of strain and stress distributions along z of the 2D FE models with and without an interphase ($f_v=5\%$): (a) strain distribution, (b) stress distribution.

5. Strain gradient effect

It is worth noting that both the analytical models (H–T and M–T) and the FE models are based on classical elasticity. When the strain gradient terms are large, classical elasticity may fail to appropriately describe the constitutive relation of the material. In these instances we can resort to strain gradient elasticity theory. The discrepancy shown in Fig. 4 is now explained by studying the strain gradient effect in this section.

For highly non-uniform stress–strain fields, the constitutive relation can be described by strain gradient elasticity (Aifantis, 1999; Askes and Aifantis, 2006) as:

$$\underline{\sigma}(x, y, z) = \underline{C} : \{ \underline{\varepsilon}(x, y, z) - l^2 \nabla^2 \underline{\varepsilon}(x, y, z) \}, \quad (7)$$

where $\underline{\sigma}$ is the stress tensor, \underline{C} is the stiffness tensor, $\underline{\varepsilon}$ is the strain tensor and $\nabla^2 \underline{\varepsilon}$ is a strain Laplacian. By assuming:

$$\nabla^2 \underline{\varepsilon}(x, y, z) = \underline{\kappa}(x, y, z) \circ \underline{\varepsilon}(x, y, z), \quad (8)$$

where $\underline{\kappa}$ is a second order tensor relating the components of strain gradient with strain components, ‘ \circ ’ represents the Hadamard product or entrywise product, Eqs. (7) and (8) yield²:

$$\underline{\sigma}(x, y, z) = \underline{C} : \left\{ \left(\underline{I} - l^2 \underline{\kappa}(x, y, z) \right) \circ \underline{\varepsilon}(x, y, z) \right\}, \quad (9)$$

where \underline{I} is a two dimensional tensor with all components equal one.³ Eq. (9) indicates that the strain gradient effects can be equivalent to a non-uniformly distributed effective stiffness.

² For a 1D case, Eq. (9) is simply $\sigma(x) = E[1 - l^2 \kappa(x)] \varepsilon(x) = E^{\text{effective}}(x) \varepsilon(x)$. So the effect of strain gradient can be equivalent to a material with non-uniform effective stiffness.

³ \underline{I} is different from the unit matrix.

From the 2D FE results with no interphase, the distributions of tensile strain component ε_{xx} along z in the PU matrix between clay layers can be accurately fitted by a parabola, shown in Fig. 9.

Since the strains along x are quasi-constant, $\frac{\partial^2 \varepsilon_{zz}}{\partial x^2} \approx 0$. Thus the strain Laplacian, is simplified to $\nabla^2 \varepsilon_{xx} \approx \frac{\partial^2 \varepsilon_{zz}}{\partial z^2}$ and can be calculated from the parabolas shown in Fig. 9. The distribution of $\kappa_{xx} = \nabla^2 \varepsilon_{xx} / \varepsilon_{xx}$ along z is shown in Fig. 10, which shows a rapid increase of the absolute value of the strain gradient when approaching the clay/PU interface. A similar phenomenon is observed for all volume fractions. According to Eq. (9), the area with a large absolute value of strain gradients near the interface can be equivalent to an effective interphase. It is also shown in Fig. 10 that with the decrease of volume fraction, the peaks of κ_{xx} tend to flatten, so the assumption of an effective interphase layer with constant thickness used in Section 3 is reasonable. The value of $nti=2$, i.e. $t_i=7.2$ nm calibrated in Section 3 is shown to be consistent with the strain gradient analysis, as shown in Fig. 10, in which the thickness of the shaded effective interphase area is of the same order as t_i calibrated from FE simulations.

6. Strain gradient Mori–Tanaka model

The existence of interphase layers can be due to various physical and/or chemical reasons. Analogy of the strain gradient effect and the effective interphase has been explained in Section 5. From the view of continuum mechanics, instead of adding a separate interphase in modeling, as shown in Section 3, the introduction of strain gradient elasticity to the classical composite theory can achieve a similar synergistic effect. In this section, a strain gradient Mori–Tanaka Model (SGMT) is derived by introducing the theory of strain gradient elasticity to the classical Mori–Tanaka composite model (Tandon and Weng, 1984).

When constant stresses $\bar{\sigma}_{ij}$ are applied at the boundaries, the strain field of the matrix is assumed to be uniform before adding the inclusions. The stiffness tensor of the matrix is C_{ijkl}^0 , the initial uniform strain in the matrix is ε_{kl}^0 . The stress and strain in the matrix are related as:

$$\bar{\sigma}_{ij} = C_{ijkl}^0 \varepsilon_{kl}^0. \quad (10)$$

If the inclusion is ellipsoidal, the stress and strain fields are always uniform and there is no strain gradient, the strain gradient elasticity degenerates into classical elasticity, and the classical composite theory holds. But if the inclusion is non-ellipsoidal, after adding the inclusions, the stress and strain fields in the matrix are not

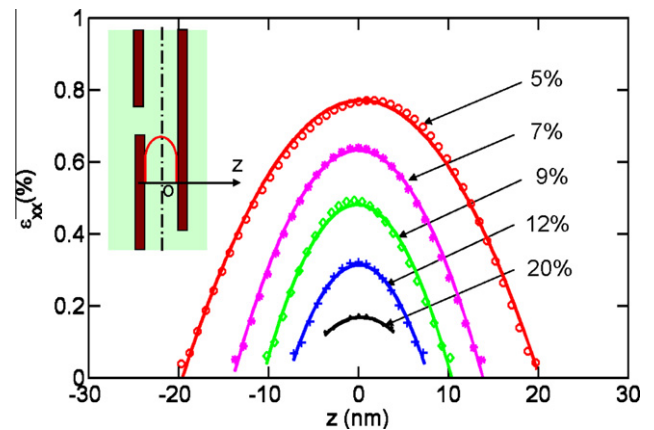


Fig. 9. Strain distributions in the PU matrix between neighboring clay layers for various volume fractions (the markers represent the data from 2D plane strain FE model with no interphase; the solid lines represent the parabola curve fitting of the FE data).

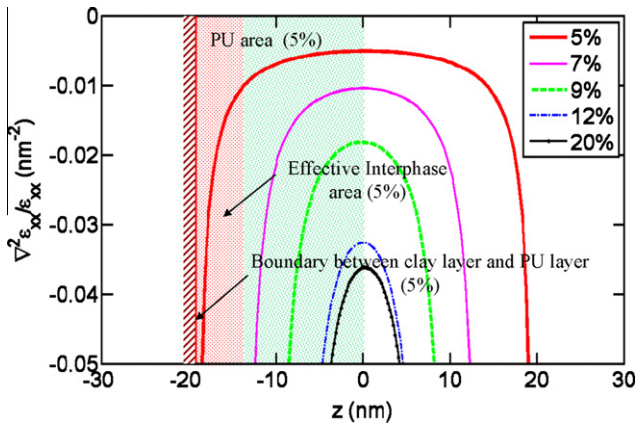


Fig. 10. Distribution of strain gradients between neighboring clay layers for 2D RVEs with no interphase (the coordinate in Fig. 7 is used).

uniform and the uniformity depends on the value of SR (Li et al., 2011), which indicates that the perturbation strain in the matrix is non-uniform. In order to distinguish this non-uniformity from the uniform cases, the notation $\langle \bullet \rangle$ is used to represent the spatial average of a field quantity. Thus the spatial average of the strain in the composite $\langle \tilde{\epsilon}_{kl} \rangle$ is related to the constant applied stress $\bar{\sigma}_{ij}$ linearly through the stiffness of the composite as:

$$\bar{\sigma}_{ij} = C_{ijkl} \langle \tilde{\epsilon}_{kl} \rangle. \quad (11)$$

The perturbation stress and strain to the matrix are described using the strain gradient elasticity theory, shown in Eq. (7). Thus, the average perturbation stress and strain relation becomes:

$$\langle \tilde{\sigma}_{ij} \rangle = C_{ijkl}^0 \left(\langle \tilde{\epsilon}_{kl} \rangle - \langle l^2 \nabla^2 \tilde{\epsilon}_{kl} \rangle \right). \quad (12)$$

where, l is the intrinsic length scale of the material determined by the material nanostructure. For the LBL nanocomposites, l should be related to the thickness of the PU matrix layer. Then the averaged stress field of the matrix after perturbation is

$$\bar{\sigma}_{ij} + \langle \tilde{\sigma}_{ij} \rangle = C_{ijkl}^0 \left(\epsilon_{kl}^0 + \langle \tilde{\epsilon}_{kl} \rangle - \langle l^2 \nabla^2 \tilde{\epsilon}_{kl} \rangle \right). \quad (13)$$

For composites with very high SRs, such as the present PU–MTM nanocomposites, the strain in the inclusions is infinitely small. Therefore, the gradient of the perturbation strain to the strain field of the inclusion ϵ_{kl}^{pt} due to the inclusion itself is neglected. Thus ϵ_{kl}^{pt} is uniform. After the perturbation, the stress in the inclusions satisfies:

$$\bar{\sigma}_{ij} + \langle \tilde{\sigma}_{ij} \rangle + \sigma_{ij}^{pt} = C_{ijkl}^1 \left(\epsilon_{kl}^0 + \langle \tilde{\epsilon}_{kl} \rangle + \epsilon_{kl}^{pt} \right) = C_{ijkl}^0 \left(\epsilon_{kl}^0 + \langle \tilde{\epsilon}_{kl} \rangle - \langle l^2 \nabla^2 \tilde{\epsilon}_{kl} \rangle \right) + \epsilon_{kl}^{pt} - \epsilon_{kl}^*, \quad (14)$$

where, C_{ijkl}^1 is the stiffness of the inclusion and σ_{ij}^{pt} is the second perturbation stress, and

$$\epsilon_{kl}^{pt} = S_{klmn} \epsilon_{mn}^*, \quad (15)$$

where S_{klmn} is the Eshelby tensor, which was derived by Tandon and Weng (1984) as a function of the aspect ratio of the inclusion and the elastic moduli of the matrix, and ϵ_{mn}^* is the eigen strain.

The total perturbation stress in both the matrix and the inclusion should be zero:

$$\langle \tilde{\sigma}_{ij} \rangle + f \sigma_{ij}^{pt} = 0, \quad (16)$$

where, f is the volume fraction of the inclusion. The total spatial average strain of the composite is obtained by the rule of mixtures:

$$\langle \tilde{\epsilon}_{kl} \rangle = \epsilon_{kl}^0 + \langle \tilde{\epsilon}_{kl} \rangle + f \epsilon_{kl}^{pt}. \quad (17)$$

Therefore, if the strain gradient terms are known, the stiffness of the composite can be solved from the system of Eqs. (11)–(13), (15)–(17). The gradient term leads to a synergistic effect of the enhancement efficiency. This effect will be evaluated quantitatively by a simplified assumption that:

$$\langle \nabla^2 \tilde{\epsilon}_{kl} \rangle = \beta \langle \tilde{\epsilon}_{kl} \rangle. \quad (18)$$

Using Eqs. (18), (12) becomes:

$$\langle \tilde{\sigma}_{ij} \rangle = C_{ijkl}^0 (a \langle \tilde{\epsilon}_{kl} \rangle), \quad (19)$$

where, $a = 1 - \beta l^2$. The influence of the strain gradient term can be modeled by the scalar parameter a . Eq. (13) becomes:

$$\bar{\sigma}_{ij} + \langle \tilde{\sigma}_{ij} \rangle = C_{ijkl}^0 (\epsilon_{kl}^0 + a \langle \tilde{\epsilon}_{kl} \rangle). \quad (20)$$

Eq. (14) becomes:

$$\begin{aligned} \bar{\sigma}_{ij} + \tilde{\sigma}_{ij} + \sigma_{ij}^{pt} &= C_{ijkl}^1 (\epsilon_{kl}^0 + \langle \tilde{\epsilon}_{kl} \rangle + \epsilon_{kl}^{pt}) \\ &= C_{ijkl}^0 (\epsilon_{kl}^0 + a \langle \tilde{\epsilon}_{kl} \rangle + \epsilon_{kl}^{pt} - \epsilon_{kl}^*). \end{aligned} \quad (21)$$

By solving Eqs. (20), (21) and (16), the normal eigen-strains can be implicitly written as:

$$\begin{bmatrix} D_1 & 1 & 1 \\ 1 & D_1 & 1 \\ 1 & 1 & D_1 \end{bmatrix} \begin{bmatrix} \epsilon_{11}^0 \\ \epsilon_{22}^0 \\ \epsilon_{33}^0 \end{bmatrix} + \begin{bmatrix} B_1 & B_2 & B_2 \\ B_3 & B_4 & B_5 \\ B_3 & B_5 & B_4 \end{bmatrix} \begin{bmatrix} \epsilon_{11}^* \\ \epsilon_{22}^* \\ \epsilon_{33}^* \end{bmatrix} = 0, \quad (22)$$

where

$$\begin{aligned} B_1 &= cD_a + D_2 + (D_1 - fD_a)S_{1111} + 2(1 - f_a)S_{2211}, \\ B_2 &= f_a + D_3 + (D_1 - fD_a)S_{1122} + (1 - f_a)(S_{2222} + S_{2233}), \\ B_3 &= f_a + D_3 + (1 - f_a)S_{1111} + (D_1 - fD_a + 1 - f_a)S_{2211}, \\ B_4 &= cD_a + D_2 + (1 - f_a)(S_{1122} + S_{2233}) + (D_1 - fD_a)S_{2222}, \\ B_5 &= f_a + D_3 + (1 - f_a)(S_{1122} + S_{3333}) + (D_1 - fD_a)S_{2233}, \end{aligned} \quad (23a)$$

D_1 , D_2 , D_3 are identical to the expressions given in Tandon and Weng's (1984), paper and

$$D_a = \frac{(\frac{\lambda_1}{a} - \lambda_0)}{\lambda_1 - \lambda_0} + \frac{2(\frac{\mu_1}{a} - \mu_0)}{\lambda_1 - \lambda_0}, \quad (23b)$$

$$f_a = f \frac{(\frac{\lambda_1}{a} - \lambda_0)}{(\lambda_1 - \lambda_0)}, \quad (23c)$$

where λ_0 , μ_0 , and λ_1 , μ_1 are the Lamé constants of the matrix and the inclusion, respectively. The normal eigen strains can be written explicitly as:

$$[\epsilon_{11}^*, \epsilon_{22}^*, \epsilon_{33}^*] = [b_{11}, b_{22}, b_{33}] \epsilon_2^0, \quad (24a)$$

where

$$\begin{aligned} b_{11} &= (-A_1 v_0 - A_2 + A_2 v_0) / A, \\ b_{22} &= \frac{-2v_0 A_3 + (1 - v_0) A_4 + (1 + v_0) A_5 A}{2A}, \\ b_{33} &= \frac{-2v_0 A_3 + (1 - v_0) A_4 - (1 + v_0) A_5 A}{2A}, \end{aligned} \quad (24b)$$

where A_1 , A_2 , A_3 , A_4 , A_5 and A are again provided as given by Tandon and Weng (1984). The total spatial average strain is

$$\langle \tilde{\epsilon}_{kl} \rangle = (1 - f) (\epsilon_{kl}^0 + \langle \tilde{\epsilon}_{kl} \rangle) + f (\epsilon_{kl}^0 + \langle \tilde{\epsilon}_{kl} \rangle + \epsilon_{kl}^{pt}). \quad (25)$$

Therefore, the components of the stiffness matrix can be solved.

This strain gradient M–T model is applied to the present PU–MTM nanocomposites. First, assuming the parameter of strain gradient a is a constant independent of volume fraction, by taking $a = 0.04$, the SGMT prediction is compared with experiments and classical elasticity models in Fig. 11(a). Physically, the strain gradient effects can be analogous to an interphase area with gradually

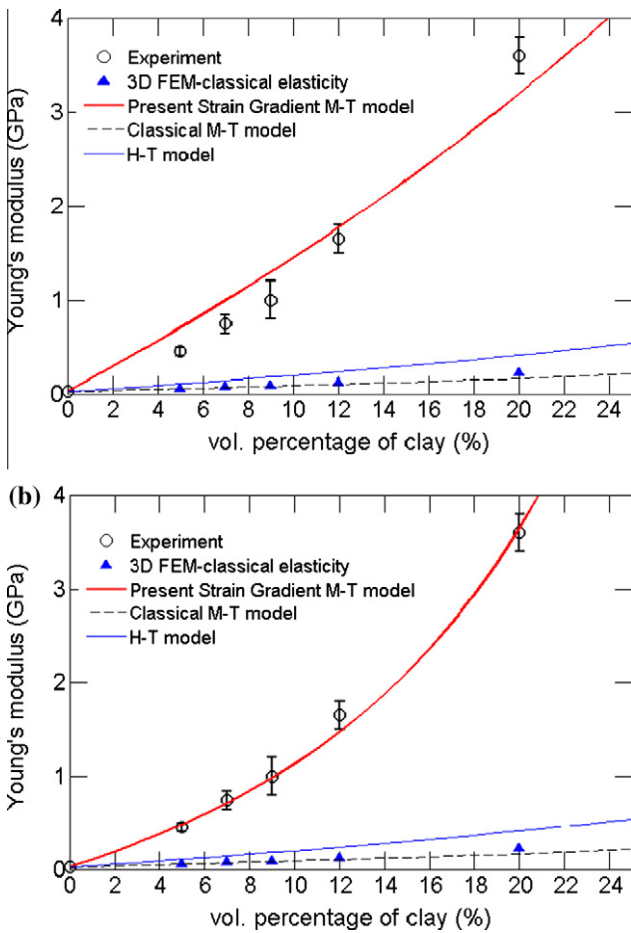


Fig. 11. Comparison of prediction results of strain gradient M-T model and other models with experimental data for LBL PU-MTM nanocomposite: (a) $a = 0.04$, (b) $a_0 = 0.07$, $H = -0.17$.

changing properties or multiple uniform interphase layers. Conceptually, the SGMT can model this gradual change of interphase area by introducing the strain gradient term to the perturbation stress and strain relation (Eq. 21), which is more realistic than the all interphase MT model. Therefore better results are obtained by the SGMT model shown in Fig. 11(a) than the all interphase MT model shown in Fig. 5 at relatively high volume fractions. Next, the strain gradient parameter a is assumed to be a continuous function of volume fraction f , $a = a(f)$. First, let us assume a linear function $a = a_0 + Hf_p$, by taking $a_0 = 0.07$, $H = -0.17$, the SGMT model captures the stiffness of all specimens more accurately, as shown in Fig. 11(b). The negative H indicates qualitatively that the contribution of a strain gradient term should increase with increasing volume fraction. Also, it indicates that the function of $a(f)$ should have a singularity at zero volume fraction, otherwise a_0 should be very close to 1 to degenerate to the classical MT model at zero volume fraction.

Also, strain gradients are a source of particle size effects in nanocomposites, as illustrated in Fig. 12, the spatial average ' $\langle \cdot \rangle$ ' can be expressed in the coordinates of isolines/isosurfaces of function ' \cdot ' around the particles as:

$$\langle \cdot \rangle = \frac{f}{(1-f)} \frac{\int(\cdot)S(r)dr}{V_p}, \quad (26)$$

where r is the coordinate representing the distances between a isolate/isosurface and the particle surface. $S(r)$ is the circumference of the isolate or the area of the isosurface.

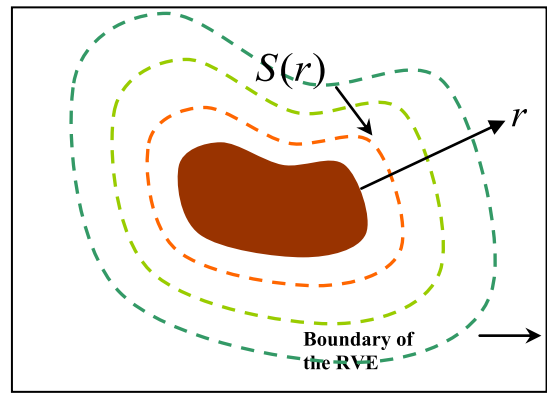


Fig. 12. Sketch of the coordinates of isolines/isosurfaces around a particle.

Eq. (26) conceptually shows how the spatial average of fields depends on a generalized surface-to-volume ratio $\frac{\int(\cdot)S(r)dr}{V_p}$, which is particle size dependent. Therefore, the SGMT model is particle size-dependent. It was shown by Li et al. (2011) that interphase can account for particle size effects of nanocomposites. In a real nanocomposite, both the interphase and the strain gradient can contribute to the stiffness enhancement mechanism and size effects simultaneously.

7. Conclusion

New mechanics models that describe the synergistic effects of LBL polymer/clay nanocomposites, and which use either a physical interphase or one caused by the presence of strain gradients, have been presented. It is shown that both effects are critical to understanding and evaluating the stiffness enhancement efficiency of nanocomposites, from a continuum mechanics modeling view point. Both approaches are applied to a LBL polyurethane–montmorillonite (PU-MTM) clay nanocomposite. Good correlation between the predictions and experimental results are shown.

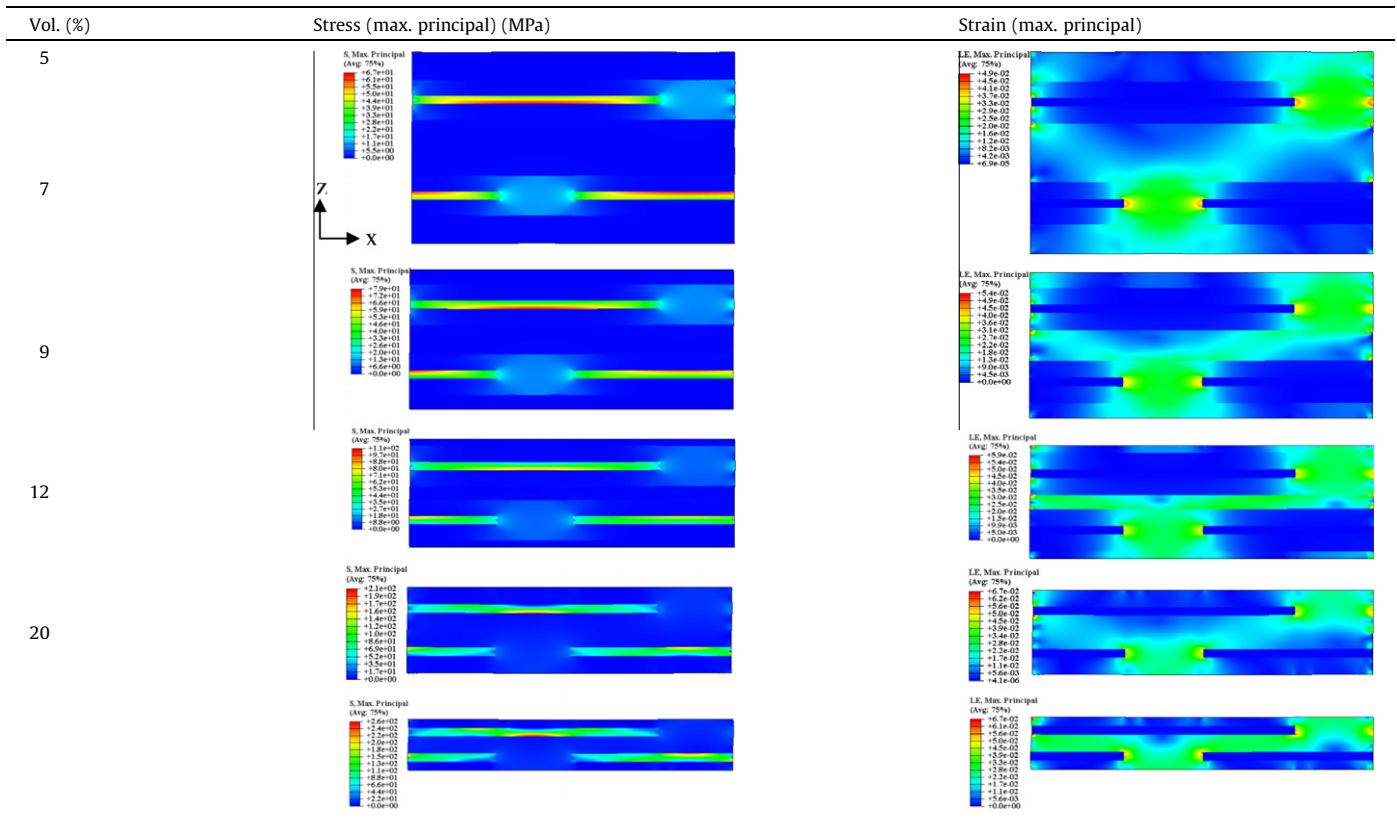
The nanostructure of the LBL PU/MTM is analysed, and the process of determining the dimensions of the nanostructure is illustrated. An inverse method to determine the interphase thickness and its stiffness using 2D plane strain and 3D finite element simulations of the nanostructures is illustrated by choosing an unsymmetric RVE appropriately. An iteration process of calibrating and validating the interphase features by 2D FE simulations and 3D FE simulations is shown. Using the calibrated interphase feature, both 2D plane strain and 3D FE simulations can predict the stiffness of PU-MTM nanocomposites with various volume fractions. How the interphase controls the load transfer between the matrix and filler and the strain gradient effect are addressed by analyzing the strain and stress distributions in the 2D RVE from the FE results.

A strain gradient Mori–Tanaka (SGMT) model is developed by introducing strain gradient elasticity theory to the M–T model. A simplification is made to study the strain gradient effect by relating strain gradients to the strain through a parameter a . By assuming that a is linearly related to the volume fraction of clay, the strain gradient M–T model can capture all the experimental data measured by our group accurately. The size-dependency of the strain gradient M–T model is addressed conceptually. An analogy between the strain gradient effect and the interphase to account for the synergistic effects and size effects of nanocomposites is provided.

Acknowledgment

The authors are grateful for financial sponsorship from the Office of Naval Research through Grant No. #N00014-06-1-0473.

Table 1
2D FE results $nEi = 17$, $nti = 2$, $\Delta^a = 1$ nm ($\epsilon_{xx} \approx 0.7\%$).



^a Δ is the controlled displacement at the boundary of the right hand side of RVEs in the tensile direction.

Table 2
3D FE results, $nEi = 17$, $nti = 2$, $\Delta = 1$ nm ($\epsilon_{xx} \approx 0.7\%$).

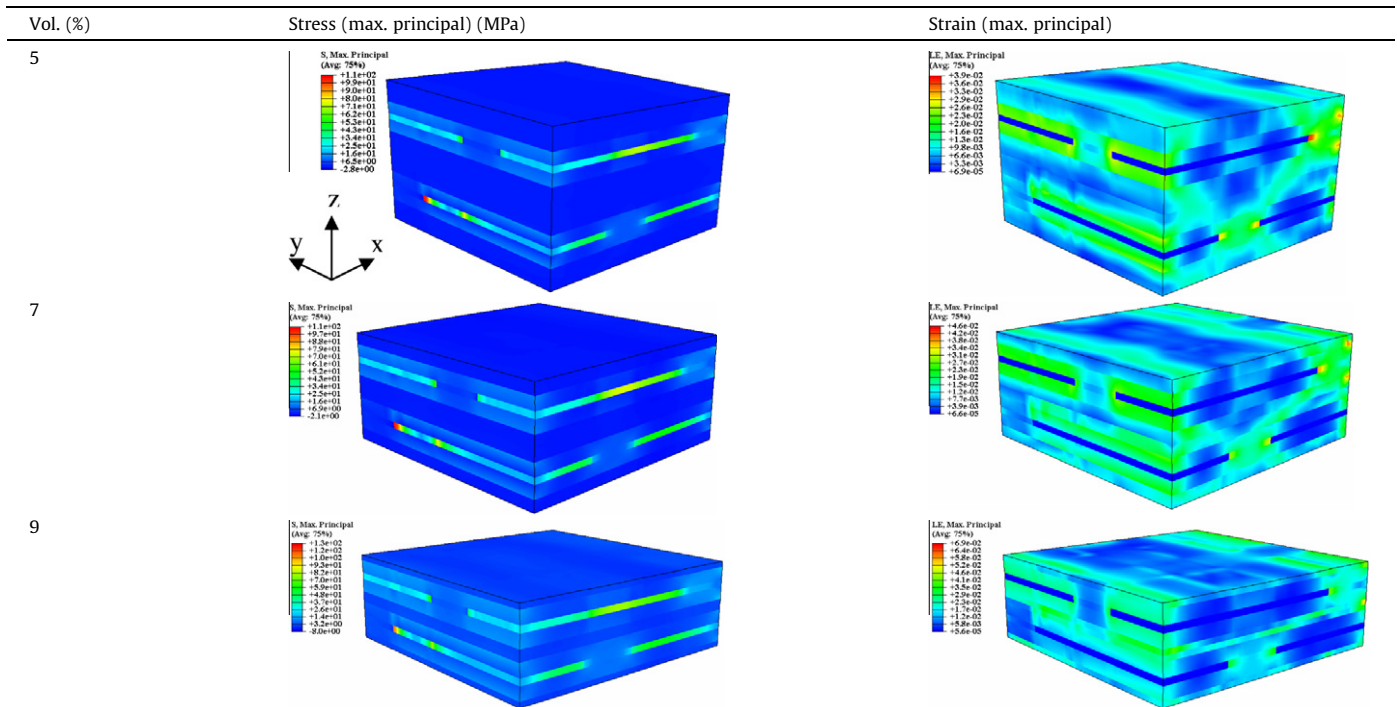
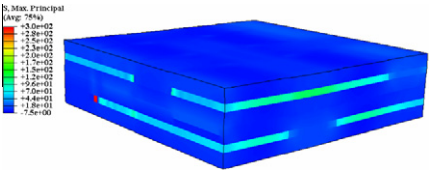
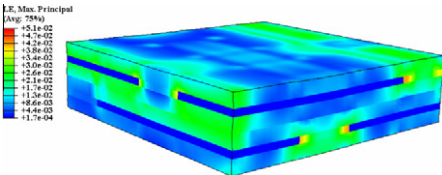
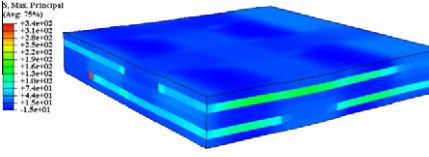
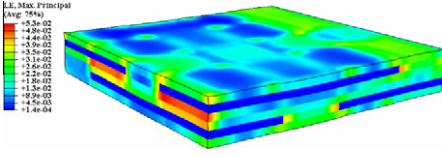


Table 2 (continued)

Vol. (%)	Stress (max. principal) (MPa)	Strain (max. principal)
12		
20		

Appendix. Contours of strain and stress distribution of 2D and 3D FE simulations

See Tables 1 and 2.

References

- ABAQUS, 2006. User's Manual, version 6.6. Hibbit, Karlsson and Sorensen Inc.
- Aifantis, E.C., 1999. Strain gradient interpretation of size effects. *International Journal of Fracture* 95, 299–314.
- Askes, H., Aifantis, E.C., 2006. Gradient elasticity theories in statics and dynamics – a unification of approaches. *International Journal of Fracture* 139, 297–304.
- Barthelat, F., Tahng, H., Zavattieri, P.D., Li, C.-M., Espinosa, H.D., 2007. On the mechanics of mother-of-pearl: a key feature in the material hierarchical structure. *Journal of the Mechanics and Physics of Solids* 55, 306–337.
- Baschnagel, J., Binder, K., 1995. On the influence of hard walls on structural properties in polymer glass simulation. *Macromolecules* 28, 6018–6808.
- Bažant, Z.P., Cedolin, L., 1991. *Stability of Structures*. Oxford University Press, Inc.
- Bertoldi, K., Boyce, M.C., Deschanel, S., Prange, S.M., Mullin, T., 2008. Mechanics of deformation-triggered pattern transformations and superelastic behavior in periodic elastomeric structures. *Journal of the Mechanics and Physics of Solids* 56 (8), 2642–2668.
- Ciprari, D., Jacob, K., Tannenbaum, R., 2006. Characterization of polymer nanocomposite interphase and its impact on mechanical properties. *Macromolecules* 39, 6565–6573.
- Cosoli, P., Scocchi, G., Priol, S., Fermeglia, M., 2008. Many-scale molecular simulation for ABS-MMT nanocomposites: upgrading of industrial scraps. *Microporous and Mesoporous Materials* 107, 169–179.
- Dunn, I.S., Anderson, L.R., Kiefer, F.W., 1980. *Fundamentals of Geotechnical Analysis*. John Wiley and Sons, New York, NY.
- Eringen, A.C., 1972. Linear theory of nonlocal elasticity and dispersion of plane waves. *International Journal of Engineering Science* 10 (5), 425–435.
- Eringen, A.C., Edelen, D.G.B., 1972. On nonlocal elasticity. *International Journal of Engineering Science* 10, 233–248.
- Fertig III, R.S., Garnich, M.R., 2004. Influence of constituent properties and microstructural parameters on the tensile modulus of a polymer/clay nanocomposite. *Composites Science and Technology* 64, 2577–2588.
- Fossey, S., 2002. Atomistic modeling of polymer matrices in nanocomposites. In: *Nanocomposites 2002: Delivering New Value to Polymers Conference Proceedings*. Executive Conference Management, San Diego, CA.
- Ginzburg, V.V., Balazs, A.C., 1999. Calculating phase diagrams of polymer-platelet mixtures using density functional theory: implications for polymer/clay composites. *Macromolecules* 32, 5681–5688.
- Halpin, J.C., 1969. Stiffness and expansion estimates for oriented short fiber composites. *Journal of Composite Materials* 3, 732–734.
- Halpin, J.C., Kardos, J.L., 1976. The Halpin-Tsai equations: a review. *Polymer Engineering Science* 16 (5), 344–352.
- Hbaieb, K., Wang, Q.X., Chia, Y.H.J., Cotterell, B., 2007. Modelling stiffness of polymer/clay nanocomposite. *Polymer* 48, 901–909.
- Helfand, E., Tagami, Y., 1972. Theory of the interface between immiscible polymers. II. *Journal of Chemistry and Physics* 56, 3592–3601.
- Kaushik, A.K., Podsiadlo, P., Qin, M., Shaw, C.M., Waas, A.M., Kotov, N.A., Arruda, E.M., 2009. The role of nanoparticle layer separation in the finite deformation response of layered polyurethane-clay nanocomposites. *Macromolecules* 42 (17), 6588–6955.
- Li, Y., Kaushik, A.K., Waas, A.M., Podsiadlo, P., Kotov, N.A., Arruda, E.M., 2008a. Study of enhancement mechanism and synergistic effects of polymer/clay nanocomposite. In: *6th International Conference on Mechanics of Time-Dependent Materials (MTDM)*, Paper 43, Curran Associates Inc, ISBN: 9781605601120.
- Li, Y., Waas, A.M., Arruda, E.M., 2008b. A particle size-shape-dependent three-phase two-step Mori-Tanaka method for studying of the interphase and particle size and shape effects of polymer/clay nanocomposites. In: *Proceedings of 2008 ASME International Mechanical Engineering Congress and Exposition (IMECE)*, vol. 13, pp. 225–232.
- Li, Y., Waas, A.M., Arruda, E.M., 2008c. A non-local visco-plastic model with strain gradient effects and interphase effects for simulating the stiffness and yield strength of a class of polymer nanocomposites. In: *Proceedings of 2008 ASME International Mechanical Engineering Congress and Exposition (IMECE)*, vol. 13, pp. 1119–1126.
- Li, Y., Waas, A.M., Arruda, E.M., 2011. A closed-form, hierarchical, multi-interphase composite model—derivation, verification and application. *Journal of Mechanics and Physics of Solids* 59 (1), 43–63.
- Lipatov, Y.S., Nesterov, A.E., 1997. *Thermodynamics of Polymer Blends*, first ed.. Polymer Thermodynamics Library, vol. 1 Technomic Publishing.
- Liu, R.Y.F., Bernal-Lara, T.E., et al., 2004. Interphase materials by forced assembly of glassy polymers. *Macromolecules* 37, 6972–6979.
- Liu, H., Brinson, L.C., 2006. A hybrid numerical-analytical method for modeling the viscoelastic properties of polymer nanocomposites. *Transactions of the ASME* 73, 758–768.
- Liu, H., Brinson, L.C., 2008. Reinforcing efficiency of nanoparticles: a simple comparison for polymer nanocomposites. *Composite Science and Technology* 68, 1502–1512.
- Manevitch, O.L., Rutledge, G.C., 2004. Elastic properties of a single lamella of montmorillonite by molecular dynamics. *Journal of Physical Chemistry B* 108, 1428–1435.
- Mori, T., Tanaka, K., 1973. Average stress in matrix and average elastic energy of materials with misfitting inclusions. *Acta Metallurgica et Materialia* 21, 571–574.
- Podsiadlo, P., Kaushik, A.K., Arruda, E.M., Waas, A.M., Shim, B.S., Xu, J., Nandivada, H., Pumplun, B.G., Lahann, J., Ramamoorthy, A., Kotov, N.A., 2007. Ultrastrong and stiff layered polymer nanocomposites. *Science* 318, 80–83.
- Podsiadlo, P., Kaushik, A.K., Shim, B.S., Agarwal, A., Tang, Z., Waas, A.M., Arruda, E.M., Kotov, N.A., 2008. Can nature's design be improved upon high strength, transparent nacre-like nanocomposites with double network of sacrificial cross links. *Journal of Physical Chemistry B*, 14359–14363.
- Pukanszky, B., 2005. Interfaces and interphases in multicomponent materials: past, present, future. *European Polymer Journal* 41, 645–662.
- Putz, K.W., Palmeri, M.J., Cohn, R.B., Andrews, R., Brinson, C.L., 2008. Effect of cross-link density on interphase creation in polymer nanocomposites. *Macromolecules* 41, 6752–6756.
- Qi, H.J., Boyce, M.C., 2005. Stress-strain behavior of thermoplastic polyurethanes. *Mechanics of Materials* 37 (8), 817–839.
- Sheng, N., Boyce, M.C., Parks, D.M., Rutledge, G.C., Abes, J.I., Cohen, R.E., 2004. Multiscale micromechanical modeling of polymer/clay nanocomposites and the effective clay particle. *Polymer* 45, 487–506.
- Suter, J.L., Coveney, P.V.H., Greenwell, C., Thyveetil, M., 2007. Large-scale molecular dynamics study of montmorillonite clay: emergence of undulatory fluctuations and determination of material properties. *Journal of Physical Chemistry C* 111, 8248–8259.
- Tandon, G.P., Weng, G.J., 1984. The effect of aspect ratio of inclusions on the elastic properties of unidirectionally aligned composites. *Polymer Composites* 5 (4), 327–333.
- Tang, H., Barthelat, F., Espinosa, H.D., 2007. An elasto-wiscoplastic interface model for investigating the constitutive behavior of nacre. *Journal of the Mechanics and Physics of Solids* 25, 1410–1438.